Chapter 2
Molecular Dynamics Simulations of Laser-Materials Interactions: General and Material-Specific Mechanisms of Material Removal and Generation of Crystal Defects

Eaman T. Karim, Chengping Wu and Leonid V. Zhigilei

Abstract Molecular dynamics simulations of laser-materials interactions are capable of providing detailed information on the complex processes induced by the fast laser energy deposition and can help in the advancement of laser-driven applications. This chapter provides a brief overview of recent progress in the atomic- and molecular-level modeling of laser-materials interactions and presents several examples of the application of atomistic simulations for investigation of laser melting and resolidification, generation of crystal defects, photomechanical spallation, and ablation of metals and molecular targets. A particular focus of the analysis of the computational results is on revealing the general and material-specific phenomena in laser-materials interactions and on making connections to experimental observations.

2.1 Introduction

Rapid expansion of the area of practical applications of short pulse laser processing (see, e.g., Chaps. 4, 5, 7, and 9 of this book) has been motivating growing interest in the fundamental mechanisms of laser-materials interactions. Computer modeling is playing an important role in the development of the theoretical understanding of laser-induced processes and the advancement of laser applications. The need for computer modeling is amplified by the complexity of the material response to the rapid laser energy deposition, which includes transient modification of the material properties by strong electronic excitation, fast non-equilibrium structural and phase transformations occurring under conditions of extreme overheating/undercooling and ultrahigh deformation rates, generation of crystal defects, photomechanical fracture and spallation, vaporization and explosive boiling of strongly overheated surface region,

E. T. Karim · C. Wu · L. V. Zhigilei (✉)
Department of Materials Science and Engineering, University of Virginia,
395 McCormick Road, P.O. Box 400745, Charlottesville, VA 22904-4745, USA
e-mail: lz2n@virginia.edu

V. P. Veiko and V. I. Konov (eds.), *Fundamentals of Laser-Assisted Micro- and Nanotechnologies*, Springer Series in Materials Science 195,
DOI: 10.1007/978-3-319-05987-7_2,

ionization and plasma formation. Computational description of this diverse range of processes is challenging and requires a combination of different computational approaches, ranging from quantum mechanics based (*ab initio*) electronic structure calculations [1–6], to classical molecular dynamics (MD) simulations [7–44], and to continuum-level kinetic and hydrodynamic modeling [45–54].

The continuum models, in particular, have been demonstrated to be capable of computationally efficient treatment of laser-induced processes at experimental time and length-scales and have been actively used for optimization of irradiation conditions in laser processing applications. Several examples of continuum-level simulations of the phase transformations occurring in laser processing of metal targets are provided in Chap. 3 of this book. The predictive power of continuum modeling, however, is limited by the need for *a priory* knowledge of all the processes that may take place during the simulations. The highly non-equilibrium nature of the processes induced by short pulse laser irradiation challenges the basic assumptions of the continuum models that are commonly designed based on equilibrium material behavior and properties.

An alternative computational approach, free of assumptions on the nature of laser-induced processes and capable of providing atomic-level insights into rapid structural and phase transformations, is presented by the classical MD simulation technique. The MD technique is based on the numerical integration of the classical equations of motion for all atoms or molecules in the system. The interatomic interaction is described by a potential energy function that defines the equilibrium structure and thermodynamic properties of the material. The main strength of the MD method is that it does not require any assumptions about the processes taking place in the systems that are investigated. This characteristic of the MD technique presents a significant advantage over the continuum-level methods where all relevant processes have to be known and described mathematically before the simulations can be performed.

The main limitations of MD method are the relatively small time- and length-scales accessible for atomic-level simulations that, even with the use of high-performance parallel computers, are typically limited to tens of nanoseconds and hundreds of nanometers. The effect of the severe limitations on the time- and length-scales of the simulations can be partially alleviated through an appropriate choice of boundary conditions capable of mimicking the interaction of the simulated small part of the system with the surrounding material [34, 55] or through design of coarse-grained mesoscopic computational approaches aimed at extending the time- and length-scales of the simulations [26, 34, 56].

The incorporation of a realistic description of laser coupling to the optically active states in the irradiated material and relaxation of the photo-excited states is another pre-requisite for application of MD technique to simulation of laser-materials interactions. A number of material-specific models have been developed for computational description of the laser excitation within the general framework of classical MD technique. For metals, a combined atomistic-continuum model that couples the classical MD method with a continuum-level description of the laser excitation and subsequent relaxation of the conduction-band electrons based on two-temperature

model (TTM) [57] has been developed and applied for investigation of laser melting [9–15], generation of crystal defects [16–18], photomechanical spallation and ablation [9, 12, 15, 21, 23, 24, 32, 37, 42, 44]. A number of computational approaches have also been suggested for MD simulations of laser interactions with Si, including the models based on local treatment of individual excitation events accounting for bond weakening, ionization and electron–ion recombination [27, 58], as well as stochastic treatment of carrier diffusion and scattering [35, 38]. For insulators, a continuum description of the laser coupling and generation of free electrons has been combined with MD modified to include the energy transfer from the excited electrons to ions [59, 60] and to account for local changes in interatomic interactions due to the ionization [59].

For molecular systems, a coarse-grained "breathing sphere" model accounting for the finite rate of the vibrational relaxation of photo-excited molecules has been developed [26, 34] and actively used in investigations of laser desorption, ablation, and spallation of one-component molecular targets [19, 21, 26, 29, 33, 34] and polymer solutions [31, 40, 43, 61, 62]. Recent extensions of the model include incorporation of ionization mechanisms that enables investigation of processes that control the yield of ions in matrix-assisted laser desorption/ionization (MALDI) mass spectrometry technique [63–65], addition of semi-quantitative representation of photochemical reactions [30, 34, 41, 66] and integration of a mesoscopic model for carbon nanotubes [67, 68] into the framework of the breathing sphere model for investigation of the ejection and deposition of nanotube-based films and coatings in matrix-assisted pulsed laser evaporation (MAPLE) technique [43].

The results of MD simulations of laser interactions with various materials have provided a wealth of information on the structural and phase transformations responsible for material modification and/or removal (ablation) in laser processing applications, e.g., see recent reviews [69–71]. While some of the laser-induced processes are found to be highly sensitive to the structure and thermodynamic properties of the target material, some other computational predictions appear to be surprisingly similar for systems as different as molecular solids and metals. In this chapter, we use the results of recent simulations of laser interactions with metal targets of different crystal structure, namely face-centered cubic (fcc) Ag, Ni, Al and body-centered cubic (bcc) Cr, and an amorphous molecular system to discuss the general and material-specific characteristics of laser-induced structural modification, spallation and ablation of irradiated targets. The processes responsible for the transitions between different regimes of material response to the laser irradiation are discussed first and related to the laser fluence dependence of the total ablation yield and the yield of individual (vapor-phase) atoms or molecules. The generation of crystal defects as a result of laser melting and resolidification, photomechanical spallation and phase explosion of overheated surface regions of irradiated targets are then discussed based on the simulation results obtained for different target materials and a broad range of irradiation conditions.

2.2 Physical Regimes of Laser-Material Interactions

In this section we use the results of TTM-MD simulations of a bulk Cr target irradiated by 200 fs laser pulses to discuss three distinct regimes of material response to laser irradiation: surface melting and resolidification, photomechanical spallation, and phase explosion regimes. We then compare the results obtained for Cr with the ones for Ni and molecular targets and discuss the differences and similarities in these results. The interatomic interactions are described by the embedded-atom method (EAM) potentials for Cr [16] and Ni [72], whereas the molecular target is simulated with the breathing sphere model [26, 34].

The conditions leading to the transitions between the different regimes can be established based on the analysis of the evolution of temperature and pressure in the surface regions of the Cr target shown in the form of contour plots in Fig. 2.1. The absorbed laser fluence of 85 mJ/cm^2 used in the simulation illustrated in Fig. 2.1a is above the threshold for surface melting, ~50 mJ/cm^2 [16] but below the spallation threshold of ~95 mJ/cm^2 [15]. The temperature plot in Fig. 2.1a shows that the electronic excitation by the 200 fs laser pulse and the energy transfer to the lattice due to the electron-phonon coupling result in a fast lattice heating. The maximum temperature reached by 5.5 ps at a depth of 10–20 nm below the surface exceeds 3200 K, which is 37 % above the equilibrium melting temperature of the EAM Cr material, $T_m = 2332$ K [15]. At this level of superheating, the surface region undergoes a fast homogeneous melting that proceeds in a form of the fast collapse of the crystal lattice and does not involve the formation of well-defined liquid nuclei [9–11, 14]. The fast homogeneous melting of ~20 nm surface region is followed by an additional slow propagation of the melting front deeper into the target, with the maximum depth of the melted region reaching 24 nm by the time of 40 ps. The short time of the homogeneous melting under the conditions of strong superheating observed in the simulation is consistent with the results of time-resolved electron diffraction experiments [73, 74], where the melting time of several picoseconds is reported for thin Al and Au films irradiated by femtosecond laser pulses.

The temperature near the liquid-crystal interface drops below the equilibrium melting temperature by the time of 50 ps and the melting turns into epitaxial recrystallization of the melted region. The strong temperature gradient created by the laser excitation results in the fast electronic heat conduction to the bulk of the target and leads to a rapid cooling of the surface region, with the initial rate of cooling of the melted region exceeding 5×10^{12} K/s. The velocity of the solidification front increases with increasing undercooling below the melting temperature and reaches the maximum value of about 80 m/s by the time when the melting front reaches the surface of the target and the temperature at the liquid-crystal interface drops down to about $0.8T_m$. The values of the velocity of solidification front observed in the simulations are comparable to the ones estimated from pump-probe measurements performed for Ag films [75].

The rapid lattice heating during the first picoseconds after the laser pulse takes place under conditions of the inertial stress confinement [19, 21] and results in the

buildup of compressive stresses in the surface region of the irradiated target. The generation of strong compressive stresses can be seen in all pressure plots shown in Fig. 2.1. The relaxation of the compressive stresses in the presence of the free surface of the target results in the generation of a bimodal stress wave consisting of a compressive component followed by a tensile one. To simulate the propagation of the stress wave from the surface into the bulk of the target, a pressure-transmitting boundary condition [34, 55] is applied at the bottom of the MD part of the TTM-MD model. The strength of the compressive and tensile stresses generated by the laser pulses increases with increasing laser fluence and, in a simulation performed at a fluence of 106 mJ/cm^2 (Fig. 2.1b), the tensile stresses exceed the dynamic strength of the melted material causing spallation or separation of a melted layer from the target. The mechanisms of spallation, which proceeds through the nucleation, growth, coalescence, and percolation of multiple voids in a surface region of the target, are discussed in more detail in Sect. 2.4.

Further increase of the laser fluence above the spallation threshold results in the separation and ejection of multiple layers/droplets from the target and, above $\sim$275 mJ/cm^2, leads to the transition from the regime of photomechanical spallation to the regime of phase explosion. As discussed below, this transition occurs when a surface region of the irradiated target reaches and exceeds the threshold temperature at which the strongly overheated melted layer becomes thermodynamically unstable and undergoes an explosive decomposition into a mixture of vapor and liquid droplets, as shown, e.g., in Fig. 2.1c. A brief discussion of the material ejection in the phase explosion regime is provided and illustrated by snapshots from a large-scale TTM-MD simulation in Sect. 2.5. The transition from the spallation to the phase explosion regime also affects the characteristics of the pressure wave generated by the laser irradiation, Fig. 2.1. While the compressive component of the pressure wave continues to increase linearly with increasing laser fluence, the tensile component starts to decrease in the spallation and phase explosion regimes. This decrease has been attributed [12, 21] to the reduced ability of the strongly overheated part of the target to support the transient tensile stresses, as well as to the compressive ablation recoil pressure that partially cancels the tensile component of the wave.

The transitions between the regimes of surface melting, photomechanical spallation, and phase explosion can also be identified from the fluence dependence of the total ablation yield and the yield of vapor-phase atoms or molecules shown in Fig. 2.2 for the Cr target as well as for Ni and amorphous molecular targets. Despite the apparent differences between the properties of the target materials and irradiation conditions (pulse durations are 200 fs for Cr, 1 ps for Ni, and 15 ps for the molecular system), a unifying feature is the condition of stress confinement [21] that is satisfied in all three series of simulations [12, 15, 19]. Under the condition of stress confinement, the characteristic time of the laser heating of the absorbing material is shorter than the time required for the mechanical relaxation (expansion) of the heated volume, causing the generation of the stress waves (such as the ones in Fig. 2.1) and, at sufficiently high laser intensities, driving the spallation of surface layer(s).

At low laser fluences, below the spallation threshold, the material ejection from the transiently melted metal surfaces is limited to thermal desorption of just several

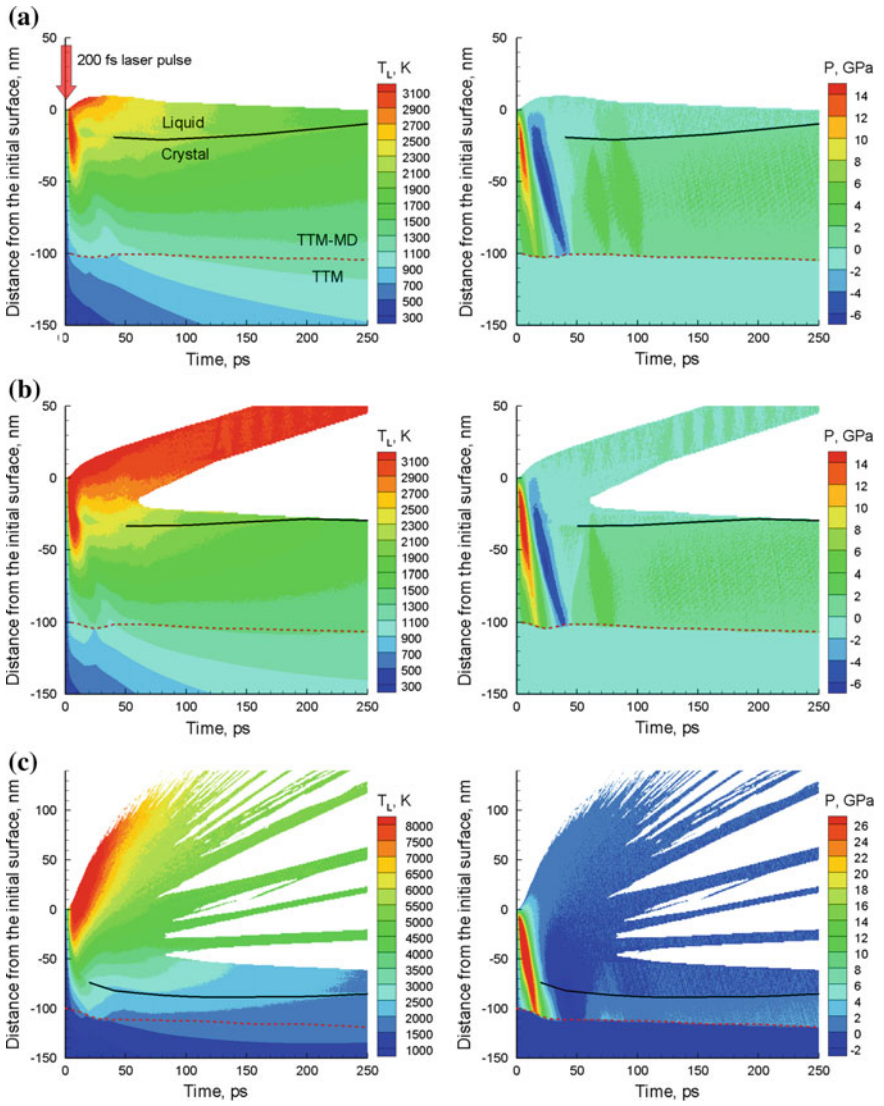

Fig. 2.1 Contour plots of the spatial and temporal evolution of lattice temperature (*left panels*) and pressure (*right panels*) in TTM-MD simulations of a bulk Cr target irradiated with a 200 fs laser pulse at absorbed fluences of 85 mJ/cm^2 (**a**), 106 mJ/cm^2 (**b**), and 298 mJ/cm^2 (**c**). The laser pulse is directed along the Y axes, from the top of the contour plots. The *black solid lines* separate the melted and crystalline regions of the target. The *red dashed lines* separate the continuum (TTM) and atomistic (TTM-MD) parts of the computational system. The results are adopted from [15]

atoms (e.g., 3 atoms evaporate from Cr target in a simulation illustrated in Fig. 2.1a). For the molecular target, the evaporation of molecules below the spallation threshold

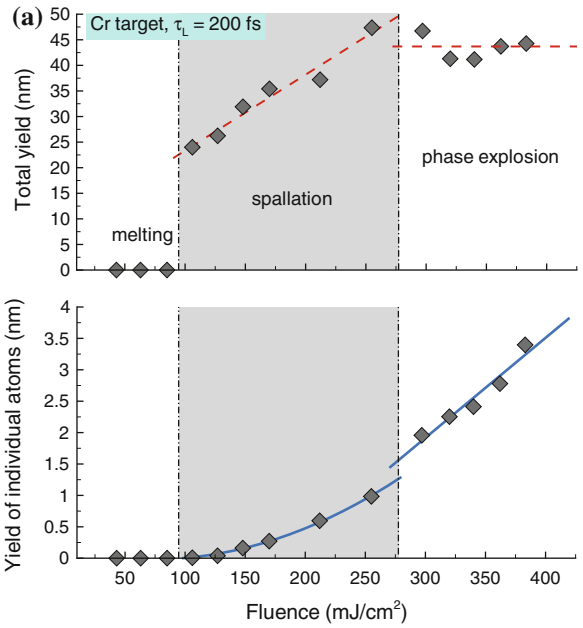

Fig. 2.2 Total ablation yield and yield of individual (vapor-phase) atoms or molecules as functions of the absorbed laser fluence predicted in TTM-MD simulations of Cr targets irradiated with 200 fs laser pulses (**a**), TTM-MD simulations of Ni targets irradiated with 1 ps laser pulses (**b**), and coarse-grained MD simulations of molecular targets irradiated with 15 ps laser pulses (**c**). The values of the total yield and yield of individual atoms/molecules are expressed in units of depth in the initial target (a layer of this depth in the initial target has the number of atoms/molecules equal to those ejected from the target). The *vertical dash-dotted lines* mark the approximate values of the threshold fluences for onset of photomechanical spallation of surface layers(s) and explosive decomposition of the surface region into vapor and liquid droplets (phase explosion). The range of fluences where the photomechanical spallation is the dominant mechanism of material ejection is highlighted by *gray color*. The *red dashed* and *blue solid curves* show the predictions of the ablation and desorption models discussed in [19, 34] in (**c**) and are guides to the eye in (**a**) and (**b**). The results for the Cr, Ni, and molecular targets are adopted from [15], [12], and [19], respectively

is more active, but still remains at a level of sub-monolayer desorption per laser pulse. In all three systems, the transition to the spallation regime manifests itself in a step increase in the total ablation yield. The increase is from 0.3 nm surface layer at 2.8 mJ/cm^2 to 13.6 nm layer at 3.1 mJ/cm^2 for molecular target (Fig. 2.2c) and from essentially zero to more than 20 nm layers for metal targets, Fig. 2.2a, b. At the same time, no abrupt changes in the yield of vapor-phase atoms or molecules are observed at the spallation threshold, thus highlighting the mechanical rather than the thermodynamic nature of the driving forces responsible for the spallation onset. As the laser fluence increases above the spallation threshold, the temperature of the surface increases and the ability of the surface region to support tensile stresses diminishes, leading to the disintegration of the overheated top melted region of the

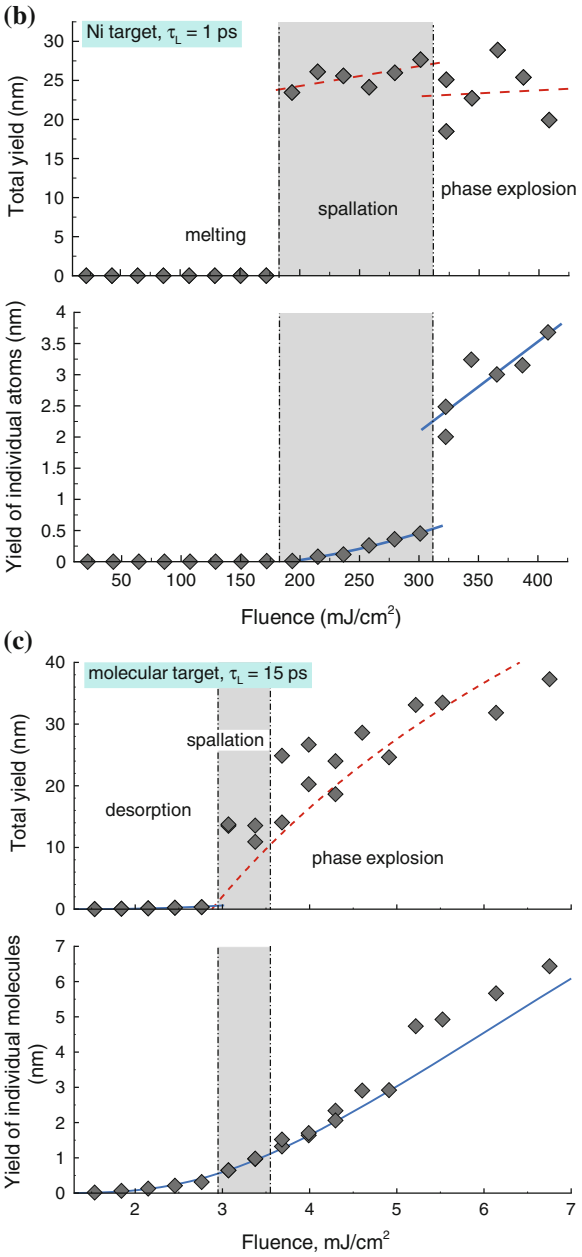

Fig. 2.2 continued

target into multiple droplets. The increase in the laser fluence in the spallation regime leads to a substantial raise of the total ablation yield for Cr, but causes only marginal or no increase of the yields for Ni and molecular targets. The number of the vapor-phase atoms or molecules in the ejected plume increases with fluence but remains below 2 % of the total yield for metal targets (Fig. 2.2a, b) and below 8 % for the molecular target (Fig. 2.2c) in the spallation regime.

Further increase of the laser fluence brings surface regions of the irradiated targets to temperatures that reach and exceed the threshold temperatures for the phase explosion [76–78] and leads to abrupt changes in the characteristics of the ablation process. The threshold temperatures for the onset of the phase explosion, T^*, have been determined in constant-pressure MD simulations of a slow heating of a metastable liquid, with zero-pressure values found to be $T^* \approx 6000$ K for the EAM Cr [15], $T^* \approx 9000$ K for the EAM Ni [12], and $T^* \approx 1060$ K for the model molecular system [40]. A surface region of the target overheated above T^* (e.g., the top region of Cr target in Fig. 2.1c) undergoes a rapid decomposition into a mixture of vapor and liquid droplets. Thus, the transition to the regime of phase explosion corresponds to the change in the dominant mechanism responsible for the material ejection from the photomechanical spallation driven by the relaxation of the laser-induced stresses to the phase explosion driven by the explosive release of the vapor. The values of the threshold fluences for the transition from spallation to the phase explosion regime also correspond to the ablation thresholds in simulations performed with longer laser pulses (e.g., 50 ps for Ni [12] and 150 ps for the molecular targets [19, 33, 34, 40]), when the condition of stress confinement is not satisfied and the spallation regime of material ejection is not activated. In these cases, direct transitions from surface evaporation to the phase explosion are observed in the simulations.

The transition to the phase explosion regime does not result in an increase in the total amount of the ejected material, Fig. 2.2. Quite the reverse, in the case of metals the total yield decreases somewhat as the fluence increases above the threshold for the phase explosion (Fig. 2.2a, b). The decrease of the total yield can be explained by two factors: (1) a higher energy cost of the decomposition of the surface region of the target into a mixture of vapor and small liquid droplets as compared to the ejection of larger droplets in the spallation regime, and (2) redeposition of some of the droplets ejected at the end of the ablation process back to the target due to the vapor pressure from the upper part of the plume. Indeed, deceleration and redeposition of some of the large droplets is observed in simulations performed for Cr and Ni at laser fluences above the thresholds for the phase explosion [12, 15]. For the molecular system, the increase in the total ablation yield in the phase explosion regime roughly follows predictions of a model that assumes the ejection of all material down to the depth in the target where a certain critical energy density is reached [19]. The prediction of this model is shown by the dashed line in Fig. 2.2c.

For metal targets, the transition to the phase explosion regime is also signified by an increase in the fraction of vapor-phase atoms in the ablation plume, from $\sim$2 % of the total yield right below the threshold for the phase explosion to 4–7 % above the threshold for Cr and from 2 % to more than 10 % of the total yield for Ni. This increase in the fraction of the vapor-phase atoms upon the transition from the

spallation to the phase explosion regimes can be related to the results of plume imaging experiments [79], where the maximum ejection of nanoparticles in laser ablation of Ni targets is observed at low fluences (possible spallation), whereas the degree of the plume atomization increases at higher fluences (possible phase explosion regime). The transition from spallation to phase explosion has also been related [12, 24] to the results of pump-probe experiments [39, 80], where the observation of optical interference patterns (Newton rings) can be explained by the spallation of a thin liquid layer from the irradiated target [21, 81] and the disappearance of the interference fringes in the central part of the laser spot [39, 82] can be related to the transition to the phase explosion regime.

2.3 Generation of Crystal Defects Below the Spallation Threshold

The discussion of the irradiation regime of melting and resolidification provided in the previous section may leave an impression of complete recovery of the initial state of the metal targets irradiated below the spallation thresholds. Detailed structural analysis of the targets that experienced the rapid melting and resolidification, however, reveals the presence of a high density of crystal defects, which may have important implications on physical, chemical, and mechanical properties of the surface layer. Two examples of defect configurations generated in surface regions of Cr and Ag targets irradiated at laser fluences that result in transient melting of about 20 nm thick layers of the targets are shown in Fig. 2.3. The simulation for Cr is the one illustrated by the contour plots shown in Fig. 2.1a and the mechanisms and kinetics of melting and resolidification in this simulation are discussed in the previous section. The simulation for Ag is performed with 100 fs laser pulse and an absorbed fluence of 70 mJ/cm^2. The interatomic interaction in Ag is described by EAM potential with parameters given in [83].

To provide a clear view of the crystal defects, the atoms that retain the original bcc or fcc local structure are blanked in the snapshots, while the remaining atoms are colored according to their potential energies in Fig. 2.3a and according to their local structure environment in Fig. 2.3b. With this visualization method, the vacancies, which are the most abundant defects introduced by the laser irradiation in these simulations, appear as clusters of atoms that surround the lattice sites with missing atoms. The distributions of vacancy concentration plotted in Fig. 2.4 indicate that most of the vacancies are located in the regions of the target that have experienced the transient melting and resolidification. To identify the mechanisms of the vacancy formation, several series of simulations of the resolidification process have been performed under well-controlled temperature and pressure conditions. These simulations reveal that most of the vacancies are generated at the rapidly advancing solidification front and are stabilized by the fast cooling of the surface region. Essentially, the vacancies are generated as “errors” made in the process of building the crystal structure at the solidification front, which, under conditions of strong

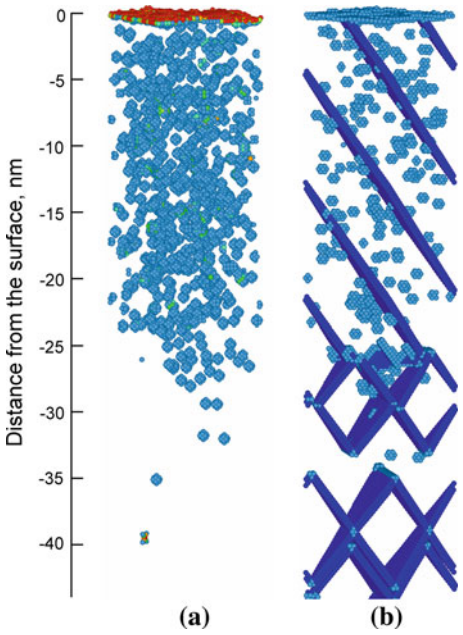

Fig. 2.3 Snapshots of the defect structures generated in surface regions of bulk bcc Cr (**a**) and fcc Ag (**b**) targets irradiated by femtosecond laser pulses at laser fluencies close to the thresholds for surface melting. The snapshots are from TTM–MD simulations performed with relatively small ($8 \times 8\,\mathrm{nm}^2$) lateral sizes of the computational cells. The laser pulse durations and absorbed fluences are 200 fs and 85 $\mathrm{mJ/cm}^2$ for Cr (**a**) and 100 fs and 70 $\mathrm{mJ/cm}^2$ for Ag (**b**). The snapshots are taken at the end of the resolidification process, at 400 ps in (**a**) and 600 ps in (**b**). The atomic configurations are quenched for 1 ps to reduce thermal noise in atomic positions and energies. The atoms are colored according to their potential energies in (**a**) and local structure environment in (**b**). The atoms that belong to local configurations with the original bcc (**a**) or fcc (**b**) structure are blanked to expose crystal defects. Each *blue ball* (a compact cluster of atoms) in the snapshots corresponds to a vacancy, a small cross at the bottom of (**a**) corresponds to an interstitial in a <110>-dumbbell configuration, and *dark blue planes* in (**b**) correspond to stacking faults with displacement vectors a/6 <112>. The results for Cr are described in [15, 16]

undercooling, moves too fast to allow for atomic rearrangements needed to correct these "errors".

While the vacancy concentrations observed in both simulations are very high (about two orders of magnitude higher than the equilibrium vacancy concentrations at the melting temperatures of Cr and Ag), the vacancy concentration in bcc Cr is about twice higher than the one in fcc Ag. Given that the energies of vacancy formation expressed in units of the thermal energy at the melting temperature, $E_v^f / k_B T_m$, are similar in the two metals (10.35 for EAM Cr and 9.88 for EAM Ag), the difference in the vacancy concentrations is likely to reflect the differences in atomic-level mechanisms responsible for the growth of the close-packed fcc and more open bcc crystal lattices.

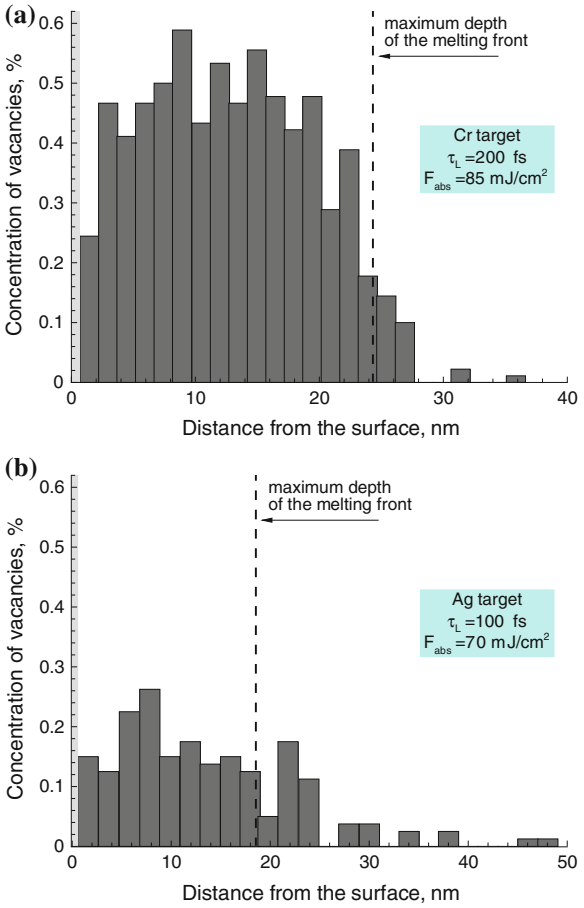

Fig. 2.4 Distribution of vacancies in the surface regions of bulk Cr (**a**) and Ag (**b**) targets irradiated by femtosecond laser pulses at laser fluencies close to the thresholds for surface melting. Snapshots of atomic configurations used in the analysis are shown in Fig. 2.3. Each bar in the histograms is the result of averaging over ten individual (001) atomic planes. The *dashed lines* mark the depths of the regions that experienced transient melting and resolidification in response to the laser irradiation

The generation of strong supersaturation of vacancies in the surface regions of the irradiated targets may have important practical implications, including the formation of nanovoids and degradation of the mechanical properties of the surface region of the target in the multi-pulse irradiation regime. The generation of vacancies in this case may be related to experimental observations of the incubation effect, when the laser fluence threshold for ablation/damage decreases with increasing number of laser pulses applied to the same area, e.g. [84–86]. The high density of vacancies generated in the surface regions of irradiated targets may also play an important

role in the redistribution of impurities or mixing/alloying in multi-component or composite targets.

In addition to vacancies, the snapshot shown in Fig. 2.3b reveals the presence of multiple stacking fault planes with displacement vectors of $a/6 <112>$, where a is the fcc lattice constant. The stacking faults located below the region that experienced the transient melting are left behind by the partial dislocations emitted from the melting front at a time when the tensile component of the laser-induced stress wave passes through the melting front. In the single crystal fcc target with {001} orientation of the irradiated surface, the partial dislocations can be activated on four different {111} slip planes. Interactions between the dislocations propagating along the different slip planes can result in the formation of immobile dislocation segments and stable dislocation configurations [71], thus leading to the hardening of the laser-treated surface. In contrast to a relatively ductile fcc Ag material, the higher resistance of bcc crystals to the movement of dislocations results in the absence of laser-generated dislocations in the bcc Cr target (Fig. 2.3a).

2.4 Evolution of Voids in Photomechanical Spallation

As discussed in Sect. 2.2 and illustrated in Fig. 2.1b, the relaxation of laser-induced stresses in the surface region of the irradiated target can generate tensile stresses that are sufficiently strong to induce cavitation and fragmentation in the melted surface region, leading to the ejection (or photomechanical spallation) of liquid layer(s) or droplets. In this section we consider the microscopic mechanisms of the spallation process and compare computational predictions obtained in simulations performed for two very different targets, an amorphous molecular solid and Ag (001) single crystal.

The visual picture of the evolution of voids in a surface region of a Ag target irradiated by a 100 fs laser pulse at a fluence of 85 mJ/cm^2, just below the spallation threshold, is shown in Fig. 2.5, where the top-view snapshots of the void evolution are shown for a relatively large-scale TTM-MD simulation performed for a system with $98.7 \times 98.7 \times 150\ nm^3$ dimensions of the atomistic part of the computational domain (84.2 million atoms). The large (by atomistic modeling standards) lateral size of the computational cell provides a clear view of the nucleation, growth and coarsening of multiple voids at a depth of ~40–60 nm under the irradiated surface and ensures that the initial evolution of voids is not affected by the periodic boundary conditions applied in the lateral directions. The appearance of voids coincides with passage of the tensile component of the stress wave through the melted surface region of the target. The voids grow as the surface layer accelerated by the initial relaxation of the laser-induced stresses moves away from the bulk of the target. In the simulation illustrated in Fig. 2.5, the outward motion of the surface layer slows down with time and reverses the direction of its motion at about 800 ps. At this time the growth of the voids turns into recession. At the same time, the fast cooling of the surface region creates conditions for fast epitaxial resolidification of the melted region, with the

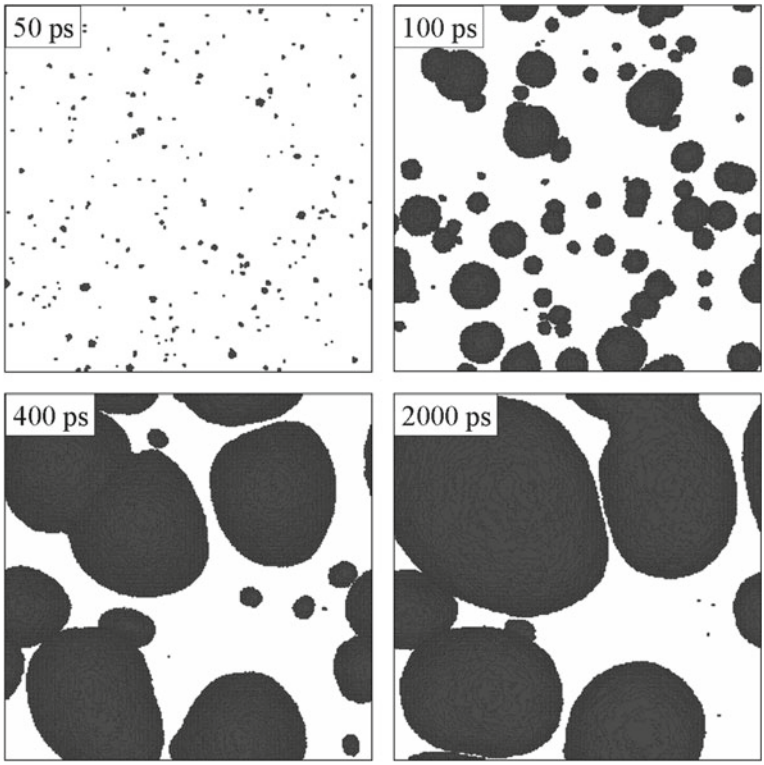

Fig. 2.5 The *top-view* snapshots of the evolution of voids (*empty space*) in the sub-surface region of a Ag (001) target irradiated by a 100 fs laser pulse at an absorbed fluence of 85 mJ/cm^2. The nucleation of voids in response to the tensile stresses associated with laser-generated stress wave (snapshot taken at 50 ps) is followed by void growth/coalescence (100 and 400 ps) and capture by the solidification front (2,000 ps)

velocity of the solidification front increasing up to 90 m/s. The solidification front crosses the region of the void evolution during the time from 500 to 1,500 ps and prevents the collapse of the voids. As a result, the voids shown in Fig. 2.5 for 2,000 ps are completely surrounded by the crystalline material and remain stable upon further cooling of the surface. At higher fluences (e.g., at 90 mJ/cm^2 for the Ag target), the expansion of voids leads to the eventual percolation of the growing empty regions and separation of liquid layer(s) or large droplets from the target.

A similar sequence of void nucleation, growth, coarsening, coalescence and percolation has been observed in earlier smaller-scale simulations performed for metals [9, 21–23, 87] and molecular systems [19, 21], as well as in recent large-scale simulations of laser spallation and ablation of Al targets [24]. In particular, an animated sequence of snapshots from a coarse-grained MD simulation of laser spallation of a molecular target posted at this web site [88] shows a picture of the void evolution that is visually similar to the one in Fig. 2.5. To quantify the evolution of voids in

laser spallation, the void size distributions are shown in Fig. 2.6a for different times during the simulation of incomplete laser spallation of Ag target discussed above and illustrated in Fig. 2.5. The distributions are fitted to power law dependences with exponents that are increasing with time, Fig. 2.6b. This increase of the power law exponent is reflecting the void coarsening and coalescence, when the size and the number of large voids are growing at the expense of quickly decreasing population of small voids. The void size distributions plotted in Fig. 2.6a are very similar not only to the distributions observed earlier in a simulation of laser spallation of a Ni film [87] and a bulk Al target [24], but also to the ones shown in Fig. 2.6c for a molecular target [21]. The time dependences of the power law exponents predicted for the two very different targets, Fig. 2.6b, d, are also very similar, except for the fact that the exponent saturates in Fig. 2.6b due to the capture of the voids by the solidification front but continues to growth in Fig. 2.6d reflecting the growth and eventual percolation of voids in the spallation of the molecular target.

The prediction of the capture of voids by the solidification front can be related to the recently reported experimental observation of surface swelling, or "frustrated ablation," in Al targets irradiated by 100 fs laser pulses [89]. Similarly to the experiments, the voids captured by the solidification front increase the volume of the surface region, leading to an effective "swelling" of the irradiated target by about 17 nm. The larger thermal conductivity and smaller melting depth near the spallation threshold in Ag, as compared to Al, makes it possible to observe this interesting phenomenon with smaller computational systems and shorter simulation times.

2.5 The Visual Picture of Phase Explosion

The transition from the spallation to the phase explosion regime of material ejection discussed in Sect. 2.2 does not result in an increase in the total amount of the ejected material (Fig. 2.2) but can still be clearly identified from changes in the composition of the ablation plume (larger fraction of vapor and small liquid droplets) and the dynamics of the plume expansion (faster expansion of the front part of the plume). These changes are the reflection of the change in the dominant driving force responsible for the material ejection from the relaxation of laser-induced stresses in the spallation regime to the explosive decomposition of material overheated up to the limit of its thermodynamic stability [12, 15, 40, 76–78] in the phase explosion regime.

The discussion of the thermodynamic conditions leading to the onset of the phase explosion provided in Sect. 2.2 and illustrated by Fig. 2.2c can be complemented by a visual picture of the material ejection in the phase explosion regime shown in Fig. 2.7. The snapshots in Fig. 2.7 are from a large-scale TTM-MD simulation of laser ablation of a bulk Al target irradiated by a 100 fs laser pulse at an absorbed fluence of 200 mJ/cm^2 [24]. The interatomic interaction in Al is described by EAM potential with parameters given in [90]. In the first snapshot, shown for 50 ps after the laser pulse, one can see a fine "Swiss cheese"-like structure of liquid cells enclosing

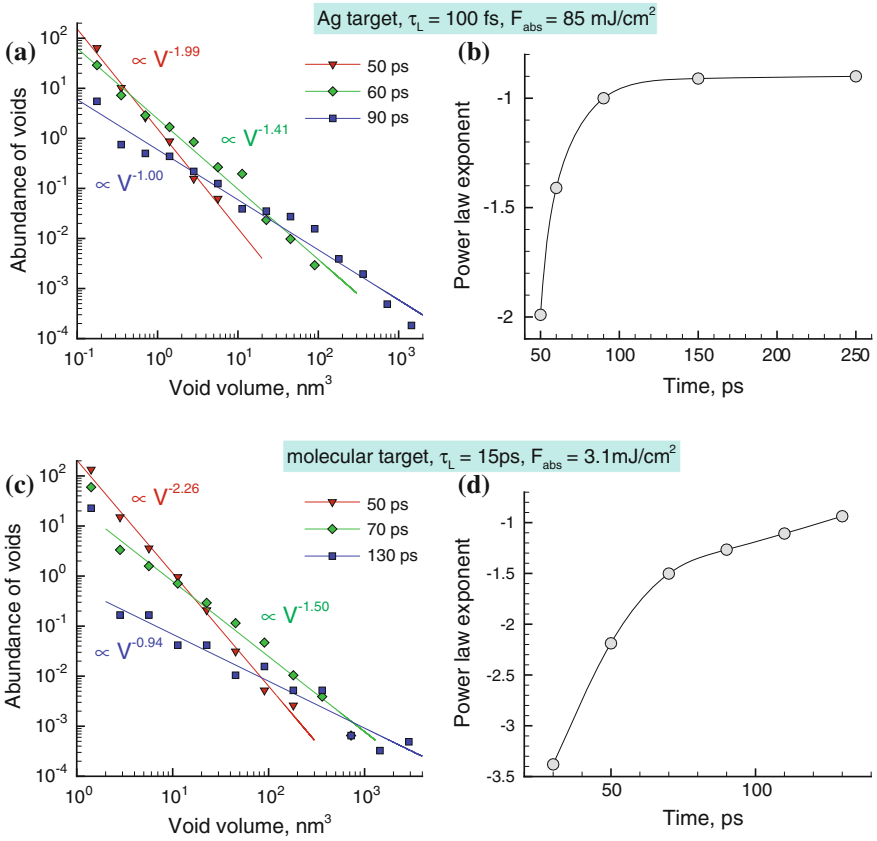

Fig. 2.6 Void abundance distributions as a function of void volume predicted for different times in simulations of short pulse laser irradiation of a single crystal Ag (001) target (**a**) and an amorphous molecular target (**c**). The *lines* in (**a**) and (**c**) are power law fits of the data points with the exponents indicated in the figures. Time dependences of the power-law exponents are shown in (**b**) and (**d**). The values of laser pulse duration, τ_L, and absorbed fluence, F_{abs}, are listed in the figure. The irradiation conditions in both simulations correspond to the regime of stress confinement. Laser fluence is just below the spallation threshold in the simulation of the Ag target and about 7 % above the spallation threshold in the simulation of the molecular target. The results for the molecular target (**c**, **d**) are adopted from [21]

dense hot vapor forming in a relatively broad surface region of the irradiated target. This cellular structure is generated by a rapid (explosive) release of vapor in the melted metal overheated above the threshold temperature for phase explosion, T^*. The expansion of the cellular structure leads to the coarsening of the liquid and vapor regions and results in the formation of a foamy structure of interconnected liquid regions surrounded by vapor, see snapshot shown for 150 ps in Fig. 2.7. Deeper into the target, the relaxation of the initial compressive pressure and the pulling force from the expanding foamy structure leads to the cavitation of the liquid and formation

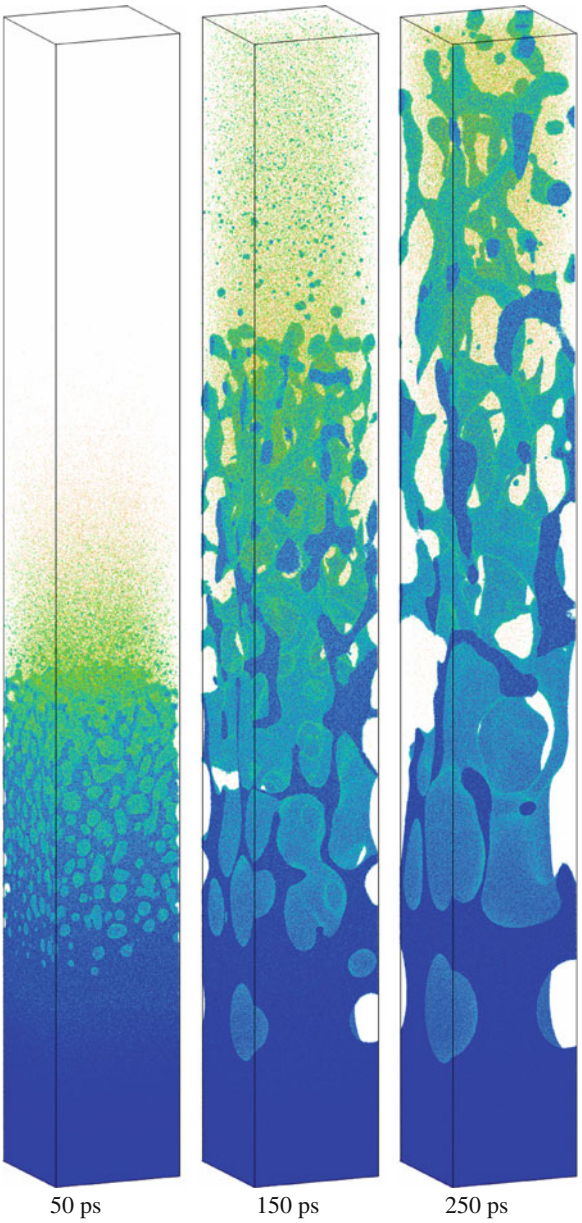

Fig. 2.7 Snapshots of atomic configurations predicted in a TTM-MD simulation of laser ablation of a bulk Al target irradiated by a 100 fs laser pulse at an absorbed fluence of 200 mJ/cm^2 [24]. Atoms are colored by their instantaneous potential energy. The initial dimensions of the atomistic (MD) part of the computational system are $94.3 \times 94.3 \times 300\,\text{nm}^3$. The irradiation regime in this simulation corresponds to the phase explosion and ablation of a surface region of the target

of coarse liquid structures extending in the direction of the plume expansion (see snapshots for 150 and 250 ps in Fig. 2.7).

The eventual decomposition of the complex hierarchical foamy structure into individual liquid droplets, clusters and vapor-phase atoms leads to the formation of a multi-component ablation plume moving away from the target. An important implication of the hierarchical ablation process illustrated in Fig. 2.7 and observed in earlier MD simulations of molecular systems [33, 91] is the effect of spatial segregation of clusters and droplets of different sizes in the ablation plume. The vapor-phase atoms/molecules and small clusters are predominantly present in the front part of the expanding plume, the medium size clusters are localized in the middle of the expanding plume, and the large liquid droplets formed at the final stage of the plume development tend to be slower and are closer to the original surface. The cluster segregation effect predicted in the simulations can be related to the results of plume imaging experiments [79, 92–95], where splitting of the plume into a fast component with optical emission characteristic for neutral atoms and a slow component with blackbody-like emission associated with presence of hot clusters is observed.

2.6 Conclusions

A comparative analysis of the results of MD simulations of laser-materials interactions performed for various target materials reveals the general and material-specific characteristics of laser-induced structural modification, spallation and ablation. The driving forces and microscopic mechanisms of laser spallation and ablation are found to be similar for a broad class of target materials. In particular, the same physical conditions are governing the onset of photomechanical spallation and the transition between the spallation and phase explosion regimes in material systems as different as metals and amorphous molecular systems. Moreover, some of the quantitative characteristics of laser-induced processes, such as the evolution of the void size distributions in spallation or the degree of segregation of clusters and liquid droplets of different sizes in ablation plumes generated in the phase explosion regime, are also surprisingly similar for different materials, reflecting the common mechanical and thermodynamic origins of the underlying processes. The material-specific predictions of the simulations include the microstructural modification of the irradiated surface, with the type and density of crystal defects generated in the melting and resolidification regime being sensitive to the structure of the target material, as well as the quantitative characteristics of the yield versus fluence dependence, which are found to be sensitive to the thermodynamic characteristics of the target material.

Given the fast advancement of the computing technology and the development of new computational models for increasingly realistic MD simulations of laser interactions with metals, semiconductors, dielectrics and organic materials, it is reasonable to expect that atomic- and molecular-level modelling will remain at the forefront of computational investigation of laser-materials interactions. The ability to simulate

increasingly larger systems is likely to open up opportunities for investigation of laser processing of multi-phase and nanocomposite systems and for establishing direct connections to experimental observations.

Acknowledgments Financial support for this work was provided by the National Science Foundation (NSF) through Grants DMR-0907247 and CMMI-1301298, Electro Scientific Industries, Inc., and the Air Force Office of Scientific Research through Grant FA9550-10-1-0541. Computational support was provided by the Oak Ridge Leadership Computing Facility (project MAT048) and NSF through the Extreme Science and Engineering Discovery Environment (project TG-DMR110090).

References

1. P.L. Silvestrelli, A. Alavi, M. Parrinello, D. Frenkel, Ab initio molecular dynamics simulation of laser melting of silicon. Phys. Rev. Lett. **77**, 3149–3152 (1996)
2. T. Dumitrica, A. Burzo, Y. Dou, R.E. Allen, Response of Si and InSb to ultrafast laser pulses. Phys. Status Solidi B **241**, 2331–2342 (2004)
3. V. Recoules, J. Clérouin, G. Zérah, P.M. Anglade, S. Mazevet, Effect of intense laser irradiation on the lattice stability of semiconductors and metals. Phys. Rev. Lett. **96**, 055503 (2006)
4. Z. Lin, L.V. Zhigilei, V. Celli, Electron-phonon coupling and electron heat capacity of metals under conditions of strong electron-phonon nonequilibrium. Phys. Rev. B **77**, 075133 (2008)
5. H.O. Jeschke, M.S. Diakhate, M.E. Garcia, Molecular dynamics simulations of laser-induced damage of nanostructures and solids. Appl. Phys. A **96**, 33–42 (2009)
6. Z. Lin, R.E. Allen, Ultrafast equilibration of excited electrons in dynamic simulations. J. Phys. Condens. Matter **21**, 485503 (2009)
7. C.F. Richardson, P. Clancy, Picosecond laser processing of copper and gold: a computer simulation study. Mol. Sim. **7**, 335–355 (1991)
8. X. Wang, X. Xu, Molecular dynamics simulation of heat transfer and phase change during laser material interaction. J. Heat Transf. **124**, 265–274 (2002)
9. D.S. Ivanov, L.V. Zhigilei, Combined atomistic-continuum modeling of short pulse laser melting and disintegration of metal films. Phys. Rev. B **68**, 064114 (2003)
10. D.S. Ivanov, L.V. Zhigilei, The effect of pressure relaxation on the mechanisms of short pulse laser melting. Phys. Rev. Lett. **91**, 105701 (2003)
11. Z. Lin, L.V. Zhigilei, Time-resolved diffraction profiles and atomic dynamics in short pulse laser induced structural transformations: molecular dynamics study. Phys. Rev. B **73**, 184113 (2006)
12. L.V. Zhigilei, Z. Lin, D.S. Ivanov, Atomistic modeling of short pulse laser ablation of metals: Connections between melting, spallation, and phase explosion. J. Phys. Chem. C **113**, 11892–11906 (2009)
13. D.A. Thomas, Z. Lin, L.V. Zhigilei, E.L. Gurevich, S. Kittel, R. Hergenröder, Atomistic modeling of femtosecond laser-induced melting and atomic mixing in Au film - Cu substrate system. Appl. Surf. Sci. **255**, 9605–9612 (2009)
14. Z. Lin, E.M. Bringa, E. Leveugle, L.V. Zhigilei, Molecular dynamics simulation of laser melting of nanocrystalline Au. J. Phys. Chem. C **114**, 5686–5699 (2010)
15. E.T. Karim, Z. Lin, L.V. Zhigilei, Molecular dynamics study of femtosecond laser interactions with Cr targets. AIP Conf. Proc. **1464**, 280–293 (2012)
16. Z. Lin, R.A. Johnson, L.V. Zhigilei, Computational study of the generation of crystal defects in a bcc metal target irradiated by short laser pulses. Phys. Rev. B **77**, 214108 (2008)
17. D.S. Ivanov, Z. Lin, B. Rethfeld, G.M. O'Connor, Th.J. Glynn, L.V. Zhigilei, Nanocrystalline structure of nanobump generated by localized photo-excitation of metal film. J. Appl. Phys. **107**, 013519 (2010)

18. C. Wu, D.A. Thomas, Z. Lin, L.V. Zhigilei, Runaway lattice-mismatched interface in an atomistic simulation of femtosecond laser irradiation of Ag film—Cu substrate system. Appl. Phys. A **104**, 781–792 (2011)
19. L.V. Zhigilei, B.J. Garrison, Microscopic mechanisms of laser ablation of organic solids in the thermal and stress confinement irradiation regimes. J. Appl. Phys. **88**, 1281–1298 (2000)
20. S.I. Anisimov, V.V. Zhakhovskii, N.A. Inogamov, K. Nishihara, A.M. Oparin, Yu.V. Petrov, Destruction of a solid film under the action of ultrashort laser pulse. Pis'ma Zh. Eksp. Teor. Fiz. **77**, 731 (JETP Lett. **77**, 606–610 (2003))
21. E. Leveugle, D.S. Ivanov, L.V. Zhigilei, Photomechanical spallation of molecular and metal targets: molecular dynamics study. Appl. Phys. A **79**, 1643–1655 (2004)
22. A.K. Upadhyay, H.M. Urbassek, Melting and fragmentation of ultra-thin metal films due to ultrafast laser irradiation: a molecular-dynamics study. J. Phys. D **38**, 2933–2941 (2005)
23. B.J. Demaske, V.V. Zhakhovsky, N.A. Inogamov, I.I. Oleynik, Ablation and spallation of gold films irradiated by ultrashort laser pulses. Phys. Rev. B **82**, 064113 (2010)
24. C. Wu, L.V. Zhigilei, Microscopic mechanisms of laser spallation and ablation of metal targets from large-scale molecular dynamics simulations. Appl. Phys. A **114**, 11–32 (2014)
25. E. Ohmura, I. Fukumoto, Molecular dynamics simulation on laser ablation of fcc metal. Int. J. Jpn. Soc. Precis. Eng. **30**, 128–133 (1996)
26. L.V. Zhigilei, P.B.S. Kodali, B.J. Garrison, Molecular dynamics model for laser ablation of organic solids. J. Phys. Chem. B **101**, 2028–2037 (1997)
27. R.F.W. Herrmann, J. Gerlach, E.E.B. Campbell, Ultrashort pulse laser ablation of silicon: an MD simulation study. Appl. Phys. A **66**, 35–42 (1998)
28. X. Wu, M. Sadeghi, A. Vertes, Molecular dynamics of matrix-assisted laser desorption of leucine enkephalin guest molecules from nicotinic acid host crystal. J. Phys. Chem. B **102**, 4770–4778 (1998)
29. L.V. Zhigilei, P.B.S. Kodali, B.J. Garrison, A microscopic view of laser ablation. J. Phys. Chem. B **102**, 2845–2853 (1998)
30. Y.G. Yingling, L.V. Zhigilei, B.J. Garrison, The role of photochemical fragmentation in laser ablation: a molecular dynamics study. J. Photochem. Photobiol. A **145**, 173–181 (2001)
31. T.E. Itina, L.V. Zhigilei, B.J. Garrison, Microscopic mechanisms of matrix assisted laser desorption of analyte molecules: insights from molecular dynamics simulation. J. Phys. Chem. B **106**, 303–310 (2002)
32. C. Schäfer, H.M. Urbassek, L.V. Zhigilei, Metal ablation by picosecond laser pulses: A hybrid simulation. Phys. Rev. B **66**, 115404 (2002)
33. L.V. Zhigilei, Dynamics of the plume formation and parameters of the ejected clusters in short-pulse laser ablation. Appl. Phys. A **76**, 339–350 (2003)
34. L.V. Zhigilei, E. Leveugle, B.J. Garrison, Y.G. Yingling, M.I. Zeifman, Computer simulations of laser ablation of molecular substrates. Chem. Rev. **103**, 321–348 (2003)
35. P. Lorazo, L.J. Lewis, M. Meunier, Short-pulse laser ablation of solids: from phase explosion to fragmentation. Phys. Rev. Lett. **91**, 225502 (2003)
36. N.N. Nedialkov, P.A. Atanasov, S.E. Imamova, A. Ruf, P. Berger, F. Dausinger, Dynamics of the ejected material in ultra-short laser ablation of metals. Appl. Phys. A **79**, 1121–1125 (2004)
37. C. Cheng, X. Xu, Mechanisms of decomposition of metal during femtosecond laser ablation. Phys. Rev. B **72**, 165415 (2005)
38. P. Lorazo, L.J. Lewis, M. Meunier, Thermodynamic pathways to melting, ablation, and solidification in absorbing solids under pulsed laser irradiation. Phys. Rev. B **73**, 134108 (2006)
39. M.B. Agranat, S.I. Anisimov, S.I. Ashitkov, V.V. Zhakhovskii, N.A. Inogamov, K. Nishihara, Yu.V. Petrov, V.E. Fortov, V.A. Khokhlov, Dynamics of plume and crater formation after action of femtosecond laser pulse. Appl. Surf. Sci. **253**, 6276–6282 (2007)
40. E. Leveugle, L.V. Zhigilei, Molecular dynamics simulation study of the ejection and transport of polymer molecules in matrix-assisted pulsed laser evaporation. J. Appl. Phys. **102**, 074914 (2007)
41. M. Prasad, P.F. Conforti, B.J. Garrison, On the role of chemical reactions in initiating ultraviolet ablation in poly (methyl methacrylate). J. Appl. Phys. **101**, 103113 (2007)

42. M. Gill-Comeau, L.J. Lewis, Ultrashort-pulse laser ablation of nanocrystalline aluminum. Phys. Rev. B **84**, 224110 (2011)
43. L.V. Zhigilei, A.N. Volkov, E. Leveugle, M. Tabetah, The effect of the target structure and composition on the ejection and transport of polymer molecules and carbon nanotubes in matrix-assisted pulsed laser evaporation. Appl. Phys. A **105**, 529–546 (2011)
44. X. Li, L. Jiang, Size distribution control of metal nanoparticles using femtosecond laser pulse train: a molecular dynamics simulation. Appl. Phys. A **109**, 367–376 (2012)
45. R.K. Singh, J. Narayan, Pulsed-laser evaporation technique for deposition of thin films: Physics and theoretical model. Phys. Rev. B **41**, 8843–8858 (1990)
46. A. Peterlongo, A. Miotello, R. Kelly, Laser-pulse sputtering of aluminum: Vaporization, boiling, superheating, and gas-dynamic effects. Phys. Rev. E **50**, 4716–4727 (1994)
47. J.R. Ho, C.P. Grigoropoulos, J.A.C. Humphrey, Computational study of heat transfer and gas dynamics in the pulsed laser evaporation of metals. J. Appl. Phys. **78**, 4696–4709 (1995)
48. X. Xu, G. Chen, K.H. Song, Experimental and numerical investigation of heat transfer and phase change phenomena during excimer laser interaction with nickel. Int. J. Heat Mass Transf. **42**, 1371–1382 (1999)
49. O.A. Bulgakova, N.M. Bulgakova, V.P. Zhukov, A model of nanosecond laser ablation of compound semiconductors accounting for non-congruent vaporization. Appl. Phys. A **101**, 53–59 (2010)
50. K. Eidmann, J. Meyer-ter-Vehn, T. Schlegel, S. Huller, Hydrodynamic simulation of subpicosecond laser interaction with solid-density matter. Phys. Rev. E **62**, 1202–1214 (2000)
51. J.P. Colombier, P. Combis, F. Bonneau, R. Le Harzic, E. Audouard, Hydrodynamic simulations of metal ablation by femtosecond laser irradiation. Phys. Rev. B **71**, 165406 (2005)
52. A.N. Volkov, L.V. Zhigilei, Hydrodynamic multi-phase model for simulation of laser-induced non-equilibrium phase transformations. J. Phys. Conf. Ser. **59**, 640–645 (2007)
53. M.E. Povarnitsyn, T.E. Itina, K.V. Khishchenko, P.R. Levashov, Suppression of ablation in femtosecond double-pulse experiments. Phys. Rev. Lett. **103**, 195002 (2009)
54. M.E. Povarnitsyn, T.E. Itina, P.R. Levashov, K.V. Khishchenko, Mechanisms of nanoparticle formation by ultra-short laser ablation of metals in liquid environment. Phys. Chem. Chem. Phys. **15**, 3108–3114 (2013)
55. C. Schäfer, H.M. Urbassek, L.V. Zhigilei, B.J. Garrison, Pressure-transmitting boundary conditions for molecular dynamics simulations. Comp. Mater. Sci. **24**, 421–429 (2002)
56. L.V. Zhigilei, A.N. Volkov, A.M. Dongare, in *Encyclopedia of Nanotechnology*, ed. by B. Bhushan (Springer, Heidelberg, 2012), Part 4, pp. 470–480
57. S.I. Anisimov, B.L. Kapeliovich, T.L. Perel'man, Electron emission from metal surfaces exposed to ultrashort laser pulses. Sov. Phys. JETP **39**, 375–377 (1974)
58. R. Holenstein, S.E. Kirkwood, R. Fedosejevs, Y.Y. Tsui, Simulation of femtosecond laser ablation of silicon. Proc. SPIE **5579**, 688–695 (2004)
59. Y. Wang, X. Xu, L. Zheng, Molecular dynamics simulation of ultrafast laser ablation of fused silica film. Appl. Phys. A **92**, 849–852 (2008)
60. Y. Cherednikov, N.A. Inogamov, H.M. Urbassek, Atomistic modeling of ultrashort-pulse ultraviolet laser ablation of a thin Lif film. J. Opt. Soc. Am. B **28**, 1817–1824 (2011)
61. E. Leveugle, L.V. Zhigilei, A. Sellinger, J.M. Fitz-Gerald, Computational and experimental study of the cluster size distribution in MAPLE. Appl. Surf. Sci. **253**, 6456–6460 (2007)
62. A. Sellinger, E. Leveugle, J.M. Fitz-Gerald, L.V. Zhigilei, Generation of surface features in films deposited by matrix-assisted pulsed laser evaporation: the effects of the stress confinement and droplet landing velocity. Appl. Phys. A **92**, 821–829 (2008)
63. R. Knochenmuss, L.V. Zhigilei, Molecular dynamics model of ultraviolet matrix-assisted laser desorption/ionization including ionization processes. J. Phys. Chem. B **109**, 22947–22957 (2005)
64. R. Knochenmuss, L.V. Zhigilei, Molecular dynamics simulations of MALDI: laser fluence and pulse width dependence of plume characteristics and consequences for matrix and analyte ionization. J. Mass Spectrom. **45**, 333–346 (2010)

65. R. Knochenmuss, L.V. Zhigilei, What determines MALDI ion yields? A molecular dynamics study of ion loss mechanisms. Anal. Bioanal. Chem. **402**, 2511–2519 (2012)
66. Y.G. Yingling, B.J. Garrison, Coarse-grained chemical reaction model. J. Phys. Chem. B **108**, 1815–1821 (2004)
67. L.V. Zhigilei, C. Wei, D. Srivastava, Mesoscopic model for dynamic simulations of carbon nanotubes. Phys. Rev. B **71**, 165417 (2005)
68. A.N. Volkov, L.V. Zhigilei, Mesoscopic interaction potential for carbon nanotubes of arbitrary length and orientation. J. Phys. Chem. C **114**, 5513–5531 (2010)
69. L. V. Zhigilei, Z. Lin, D.S. Ivanov, E. Leveugle, W.H. Duff, D. Thomas, C. Sevilla, S. J. Guy, Atomic/molecular-level simulations of laser-materials interactions. in *Laser-Surface Interactions for New Materials Production: Tailoring Structure and Properties*, ed. by A. Miotello, P.M. Ossi. Springer Series in Materials Science, vol. 130.(Springer, New York, 2010), pp. 43–79
70. L.V. Zhigilei, E. Leveugle, D.S. Ivanov, Z. Lin, A.N. Volkov, Molecular dynamics simulations of short pulse laser ablation: Mechanisms of material ejection and particle generation. in *Nanosized Material Synthesis by Action of High-Power Energy Fluxes on Matter* (Siberian Branch of the Russian Academy of Sciences, Novosibirsk, 2010), pp. 147–220 (in Russian)
71. C. Wu, E. T. Karim, A. N. Volkov, and L. V. Zhigilei, Atomic movies of laser-induced structural and phase transformations from molecular dynamics simulations. in *Lasers in Materials Science*, ed. by M. Castillejo, P.M. Ossi, L.V. Zhigilei. Springer Series in Materials Science, vol. 191. (Springer, New York, 2014), pp. 67–100
72. X.W. Zhou, H.N.G. Wadley, R.A. Johnson, D.J. Larson, N. Tabat, A. Cerezo, A.K. Petford-Long, G.D.W. Smith, P.H. Clifton, R.L. Martens, T.F. Kelly, Atomic scale structure of sputtered metal multilayers. Acta Mater. **49**, 4005–4015 (2001)
73. B.J. Siwick, J.R. Dwyer, R.E. Jordan, R.J.D. Miller, An atomic-level view of melting using femtosecond electron diffraction. Science **302**, 1382–1385 (2003)
74. J.R. Dwyer, R.E. Jordan, C.T. Hebeisen, M. Harb, R. Ernstorfer, T. Dartigalongue, R.J.D. Miller, Femtosecond electron diffraction: an atomic perspective of condensed phase dynamics. J. Mod. Opt. **54**, 905–922 (2007)
75. W.-L. Chan, R.S. Averback, D.G. Cahill, Y. Ashkenazy, Solidification velocities in deeply undercooled silver. Phys. Rev. Lett. **102**, 095701 (2009)
76. B.J. Garrison, T.E. Itina, L.V. Zhigilei, The limit of overheating and the threshold behavior in laser ablation. Phys. Rev. E **68**, 041501 (2003)
77. A. Miotello, R. Kelly, Laser-induced phase explosion: new physical problems when a condensed phase approaches the thermodynamic critical temperature. Appl. Phys. A **69**, S67–S73 (1999)
78. N.M. Bulgakova, A.V. Bulgakov, Pulsed laser ablation of solids: transition from normal vaporization to phase explosion. Appl. Phys. A **73**, 199–208 (2001)
79. S. Amoruso, R. Bruzzese, C. Pagano, X. Wang, Features of plasma plume evolution and material removal efficiency during femtosecond laser ablation of nickel in high vacuum. Appl. Phys. A **89**, 1017–1024 (2007)
80. K. Sokolowski-Tinten, J. Bialkowski, A. Cavalleri, D. von der Linde, A. Oparin, J. Meyer-ter-Vehn, S.I. Anisimov, Transient states of matter during short pulse laser ablation. Phys. Rev. Lett. **81**, 224–227 (1998)
81. N.A. Inogamov, Y.V. Petrov, S.I. Anisimov, A.M. Oparin, N.V. Shaposhnikov, D. von der Linde, J. Meyer-ter-Vehn, Expansion of matter heated by an ultrashort laser pulse. JETP Lett. **69**, 310–316 (1999)
82. A.A. Ionin, S.I. Kudryashov, L.V. Seleznev, D.V. Sinitsyn, Dynamics of the spallative ablation of a GaAs surface irradiated by femtosecond laser pulses. JETP Lett. **94**, 753–758 (2011)
83. S.M. Foiles, M.I. Baskes, M.S. Daw, Embedded-atom-method functions for the fcc metals Cu, Ag, Au, Ni, Pd, Pt, and their alloys. Phys. Rev. B **33**, 7983–7991 (1986)
84. P.T. Mannion, J. Magee, E. Coyne, G.M. O'Connor, T.J. Glynn, The effect of damage accumulation behaviour on ablation thresholds and damage morphology in ultrafast laser micromachining of common metals in air. Appl. Surf. Sci. **233**, 275–287 (2004)

85. S.E. Kirkwood, A.C. Van Popta, Y.Y. Tsui, R. Fedosejevs, Single and multiple shot near-infrared femtosecond laser pulse ablation thresholds of copper. Appl. Phys. A **81**, 729–735
86. G. Raciukaitis, M. Brikas, P. Gecys, M. Gedvilas, Accumulation effects in laser ablation of metals with high-repetition-rate lasers. Proc. SPIE **7005**, 70052L (2008)
87. L.V. Zhigilei, D.S. Ivanov, E. Leveugle, B. Sadigh, E.M. Bringa, Computer modeling of laser melting and spallation of metal targets, in *High-Power Laser Ablation V*, ed. by C.R. Phipps. Proc. SPIE **5448**, 505–519 (2004)
88. Animated sequences of snapshots from a MD simulation of laser spallation of a molecular target, http://www.faculty.virginia.edu/CompMat/spallation/animations/
89. J.-M. Savolainen, M.S. Christensen, P. Balling, Material swelling as the first step in the ablation of metals by ultrashort laser pulses. Phys. Rev. B **84**, 193410 (2011)
90. Y. Mishin, D. Farkas, M.J. Mehl, D.A. Papaconstantopoulos, Interatomic potentials for monoatomic metals from experimental data and *ab initio* calculations. Phys. Rev. B **59**, 3393–3407 (1999)
91. L.V. Zhigilei, Computational model for multiscale simulation of laser ablation, ed. by V.V. Bulatov, F. Cleri, L. Colombo, L.J. Lewis, N. Mousseau. *Advances in Materials Theory and Modeling-Bridging Over Multiple-Length and Time Scales* Mat. Res. Soc. Symp. Proc. **677**, AA2.1.1–AA2.1.11 (2001)
92. S. Noël, J. Hermann, T. Itina, Investigation of nanoparticle generation during femtosecond laser ablation of metals. Appl. Surf. Sci. **253**, 6310–6315 (2007)
93. T.E. Itina, K. Gouriet, L.V. Zhigilei, S. Noël, J. Hermann, M. Sentis, Mechanisms of small clusters production by short and ultra-short pulse laser ablation. Appl. Surf. Sci. **253**, 7656–7661 (2007)
94. O. Albert, S. Roger, Y. Glinec, J.C. Loulergue, J. Etchepare, C. Boulmer-Leborgne, J. Perriere, E. Millon, Time-resolved spectroscopy measurements of a titanium plasma induced by nanosecond and femtosecond lasers. Appl. Phys. A **76**, 319–323 (2003)
95. N. Jegenyes, J. Etchepare, B. Reynier, D. Scuderi, A. Dos-Santos, Z. Tóth, Time-resolved dynamics analysis of nanoparticles applying dual femtosecond laser pulses. Appl. Phys. A **91**, 385–392 (2008)